ORIGINAL PAPER

Variation in structure and Li⁺-ion migration in argyrodite-type Li_6PS_5X (X = Cl, Br, I) solid electrolytes

Prasada Rao Rayavarapu · Neeraj Sharma ·
Vanessa K. Peterson · Stefan Adams

Abstract All-solid-state rechargeable lithium-ion batteries (AS-LIBs) are attractive power sources for electrochemical applications due to their potentiality in improving safety and stability over conventional batteries with liquid electrolytes. Finding a solid electrolyte with high ionic conductivity and compatibility with other battery components is a key factor in raising the performance of AS-LIBs. In this work, we prepare argyrodite-type Li_6PS_5X (X = Cl, Br, I) using mechanical milling followed by annealing. X-ray diffraction characterization reveals the formation and growth of crystalline Li_6PS_5X in all cases. Ionic conductivity of the order of 7×10^{-4} S cm^{-1} in Li_6PS_5Cl and Li_6PS_5Br renders these phases suitable for AS-LIBs. Joint structure refinements using high-resolution neutron and laboratory X-ray diffraction provide insight into the influence of disorder on the fast ionic conductivity. Besides the disorder in the lithium distribution, it is the disorder in the S^{2-}/Cl^- or S^{2-}/Br^- distribution that we find to promote ion mobility, whereas the large I^- cannot be exchanged for S^{2-} and the resulting more ordered Li_6PS_5I exhibits only a moderate conductivity. Li⁺ ion migration pathways in the crystalline compounds are modelled using the bond valence approach to interpret the differences between argyrodites containing different halide ions.

P. R. Rayavarapu (✉) · S. Adams
Department of Materials Science and Engineering,
National University of Singapore,
Singapore 117576, Singapore
e-mail: mserpr@nus.edu.sg

N. Sharma · V. K. Peterson
Australian Nuclear Science and Technology Organisation,
The Bragg Institute,
Locked Bag 2001,
Kirrawee DC, NSW 2232, Australia

Introduction

Lithium sulphide-based glassy materials are known to show high Li⁺ conductivity and thus are promising candidates for solid electrolytes of all-solid-state lithium-ion batteries (AS-LIBs) with high safety and reliability. Despite considerable efforts to improve the Li⁺ conductivity [1–3], limited current density remains a major impediment in these systems. Argyrodites are a class of chalcogenide structures related to the mineral Ag_8GeS_6, which include various fast Ag⁺ or Cu⁺ ion conductors such as A_7PS_5X (A = Ag⁺, Cu⁺) [4]. Recently, Deiseroth et al. [5] synthesized the analogous cubic Li⁺ argyrodites with formula Li_6PS_5X (X = Cl, Br, I) and Li_7PS_6. ⁷Li-NMR relaxation and impedance experiments found intrinsic local lithium mobility in the Li–argyrodite crystals as high as 10^{-2}–10^{-3} S cm^{-1} at room temperature close to that of liquid electrolytes typically composed of $LiPF_6$ salt dissolved in various carbonates. With such high lithium mobilities, these materials may be ideal for use as solid electrolytes in lithium-ion batteries. Very recent impedance and DC polarization studies by the same group suggest significantly lower dc conductivities but high chemical diffusion coefficients for pressed pellets of various argyrodites [6]. Here, we prepare argyrodite-type Li_6PS_5X (X = Cl, Br, I) using mechanical milling followed by annealing of the samples. X-ray and neutron diffraction studies and impedance measurements are reported here to provide a deeper understanding of the correlation between structure and transport properties.

Although ion transport studies for the silver and copper thio-phosphates can be based on detailed anharmonic

structure refinements [7], no comparable in-depth studies are available for the lithium-containing compounds due to the low X-ray scattering power of lithium and phase transitions that prevent low temperature single-crystal studies. In this work, we analyse the ion transport pathways in the Li_6PS_5X (X = Cl, Br) phases using optimized empirical force fields in combination with the bond valence analysis of energy landscapes for the mobile Li^+.

Sample preparation and properties characterization

Li_6PS_5X (X = Cl, Br, I) samples were prepared by high-energy mechanical milling using an agate bowl and balls (45 ml bowl and 15 balls, each of 10 mm in diameter); crystalline Li_2S, P_2S_5 and LiX (X = Cl, Br, I) powders were used as starting materials. The samples were ground for 20 h followed by annealing at 550 °C for 5 h. Samples were pressed into pellets of 10 mm in diameter and approximately 1.5 mm in thickness for annealing. All procedures were conducted under Ar atmosphere. The annealed samples were characterized by in situ X-ray powder diffraction (XRPD) in the temperature range 30 to 600 °C using Cu K_α radiation (PANalytical, X'Pert PRO equipped with a fast linear detector). The samples were kept at a pressure of 10^{-5} m bar during the measurements. XRPD data were collected in the $2\theta°$ range 10–100° with a nominal scan rate of 120 s per step and a step size of 0.016°. Neutron powder diffraction (NPD) data were collected using the high-resolution diffractometer, Echidna, at the Australian Nuclear Science and Technology Organisation (ANSTO) with a wavelength of 1.54072(2) (determined using NBS 676 Al_2O_3 standard) Å at room temperature. Samples were sealed in 6-mm vanadium cans in an Ar-filled glove box and then transferred to the instrument for the measurement. Rietveld refinements were performed using GSAS [8, 9]. Structure refinements using combined XRPD and NPD data at room temperature were performed starting from published single-crystal XRD data by Deiseroth et al. [5]. Ionic conductivity measurements of ball-milled only and annealed samples were carried out over the temperature range from room temperature to 150 °C by impedance spectroscopy (Schlumberger Solartron SI1260) in the frequency range of 1 Hz to 10 MHz using stainless steel plates as electrodes. The samples were sealed in a 12-mm-diameter Swagelok cell and equilibrated at each temperature for 20 min. The bulk resistance, R_b, was determined from fitting parameters of an equivalent circuit consisting of C_b, R_b and a CPE where C_b represents the geometric capacitor between the electrodes, and CPE is the constant phase element due to the polarization distribution at the interface between blocking electrodes and electrolyte.

Bond valence approach

Empirical relationships between bond length, R, and bond valence, s, given by

$$s_{Li-X} = \exp\left[\left(\frac{R_0 - R}{b}\right)\right] \qquad (1)$$

are widely used in crystal chemistry to identify equilibrium atomic sites as regions within a structure, where the bond valence (BV) sum of the atom approximately equals its oxidation state. A systematic adjustment of BV parameters, b, to the bond softness, together with the inclusion of interactions beyond the first coordination shell, yields adequate estimates of non-equilibrium site BV sums. The modelling of pathways for mobile Li^+ as regions of low site energy $E(Li)$ (or of low BV sum mismatch, $|\Delta V(Li)|$) has been shown to provide a simple and reliable way of identifying transport pathways in local structure models, provided that the local structure model captures the essential structural features. While bond valences, s_{Li-X}, and hence the BV sum mismatch $|\Delta V|$ are mostly expressed in arbitrary "valence units", they may—as we have shown recently—[10–17] be linked to an absolute energy scale by expressing the bond valence as Morse-type interaction energy, E, given by:

$$E = D_0\left\{\frac{(s - s_{min})^2}{s_{min}^2} - 1\right\} = D_0\left(s_{rel}^2 - 2s_{rel}\right) \qquad (2)$$

Here, $s_{rel} = s/s_{min}$, where s_{min} represents the BV for the equilibrium distance, R_{min}. R_{min} as well as the bond-breaking energy D_0 is estimated from the tabulated BV parameters and the typical coordination number of the cation, N_C [12]. As described in more detail in our previous reports [14, 16], pathways for Li^+ can be visualized as regions enclosed by isosurfaces of constant $E(Li)$ based on a grid of $E(Li)$ values with a resolution <0.1 Å covering the unit cell. The threshold value of $E(Li)$, for which the $E(Li)$ isosurfaces form a continuous migration pathway (that includes both occupied and vacant Li sites), allows for a rough estimate of the activation energy for the Li^+ ion transport process.

Results and discussions

The XRPD patterns of ball-milled samples show partial crystallinity with peaks belonging to the Li_2S, P_2S_5 and LiX (X = Cl, Br, I) phases. Samples that have been ball-milled for up to 24 h show Bragg peaks of various phases that are still rather prominent; peaks of most phases, except Li_2S, become very broad after 40 h of ball-milling for X = Cl, Br or after 60 h of ball-milling for X = I. After

annealing, all samples yield the respective argyrodite phases with comparable crystallinity. Thus, preparation time for argyrodites has been drastically reduced when compared to the original synthesis recipe [5], which takes 7 days.

The final Li_6PS_5Cl, Li_6PS_5Br and Li_6PS_5I samples exhibit the high-symmetry aristotype argyrodite structure in space group $F\text{-}43m$. The lattice parameters of Li_6PS_5Cl, Li_6PS_5Br and Li_6PS_5I are 9.850(4), 9.980(8) and 10.142(3) Å, respectively, in good agreement with reported values. Figures 1, 2 and 3 show the simultaneously refined Rietveld fits to XRPD and NPD data of the crystalline Li_6PS_5X phases. Atomic coordinates obtained from these Rietveld refinements are summarized in Tables 1, 2 and 3.

For Li_6PS_5I, our refinements yield—in harmony with earlier literature data [5, 17]—a fully ordered arrangement of I^- on the 4a site (0, 0, 0), the "anion site 1", S^{2-} on the 4d site (3/4, 3/4, 3/4), the "anion site 2" and tetrahedral PS_4^{3-} ions on the 4b site (1/2, 1/2, 1/2) with four symmetric P–S bonds to the S(3) atom. The only local disorder in this
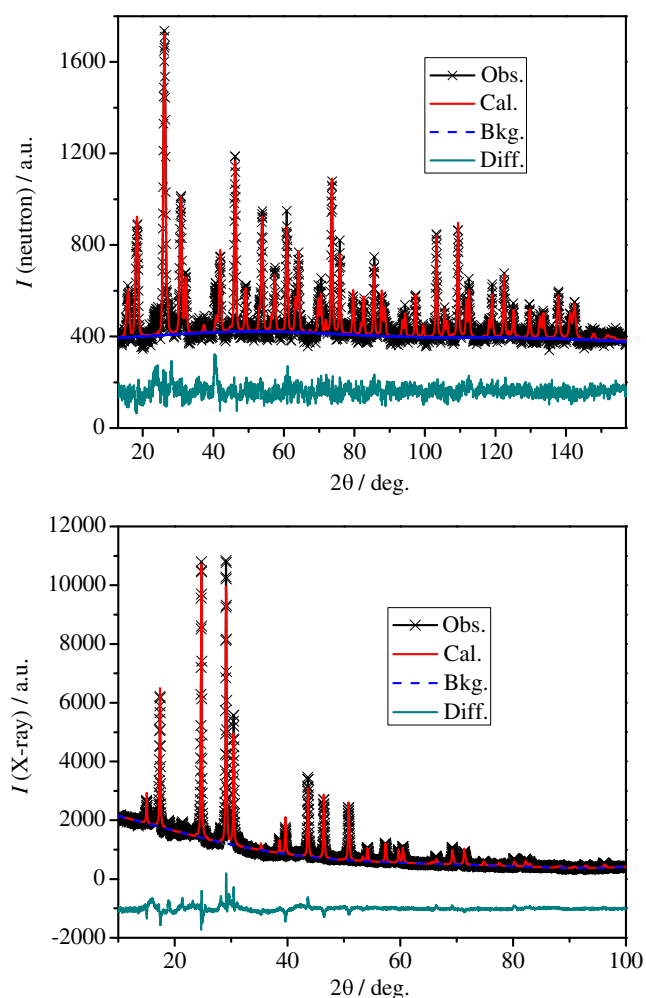

Fig. 1 Rietveld fits of simultaneously refined structural models to NPD (*top*) and XRPD (*bottom*) data for Li_6PS_5I

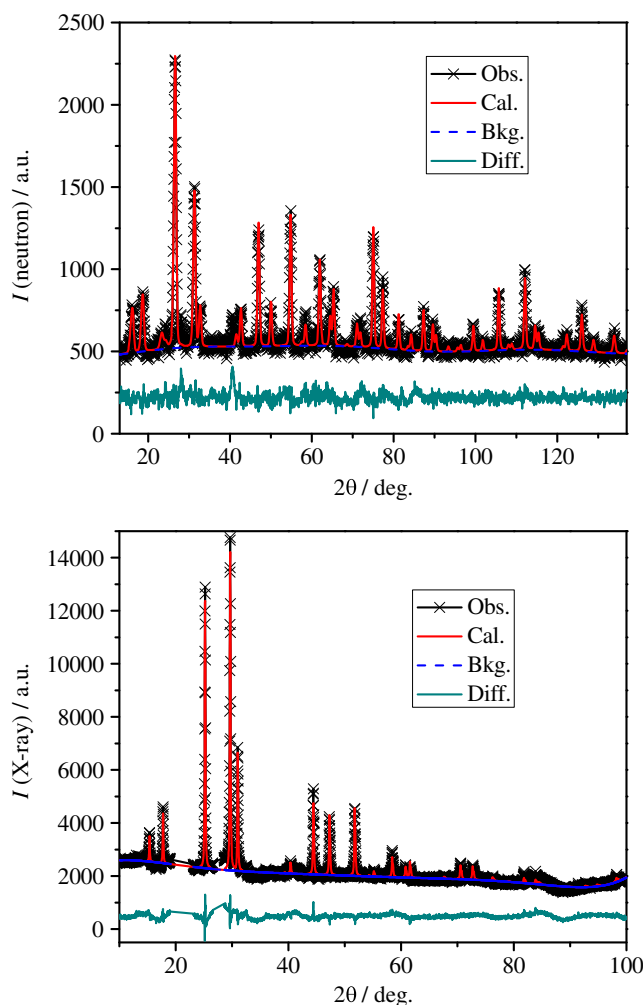**Fig. 2** Rietveld fits of simultaneously refined structural models to NPD (*top*) and XRPD (*bottom*) data for Li_6PS_5Br

structure arises from the distribution of the 24 lithium per unit cell over two partially occupied sites (Li(1) on 48h (x, x, z) and Li(2) on 24g (1/4, 1/4, z)). Each Li(2) site is surrounded by two Li(1) sites, but due to the short Li–Li distance only one of these three sites can be occupied and the Li(1)–Li(2)–Li(1) group of sites may be considered as a single, fully occupied site. Based on our harmonic refinement, ca. 15 of the 24 Li reside on the Li(1) site and ca. 9 Li occupy the Li(2) site, but a continuous distribution of lithium density with maxima on the Li(1) sites may be a more appropriate description of the local structure.

For Li_6PS_5Cl, our structure refinement assuming the same two Li(1) and Li(2) sites was not stable and a model with all 24 Li on the Li(1) site pairs was required. We note that a free refinement of the Li(1) occupancy yields a site occupancy factor SOF = 0.443, corresponding to ca. 21 Li, so that a relatively small SOF for the Li(2) site cannot be excluded. Fundamentally, the difference to the iodide case is that the Cl^- and S^{2-} ions are disordered over the "anion
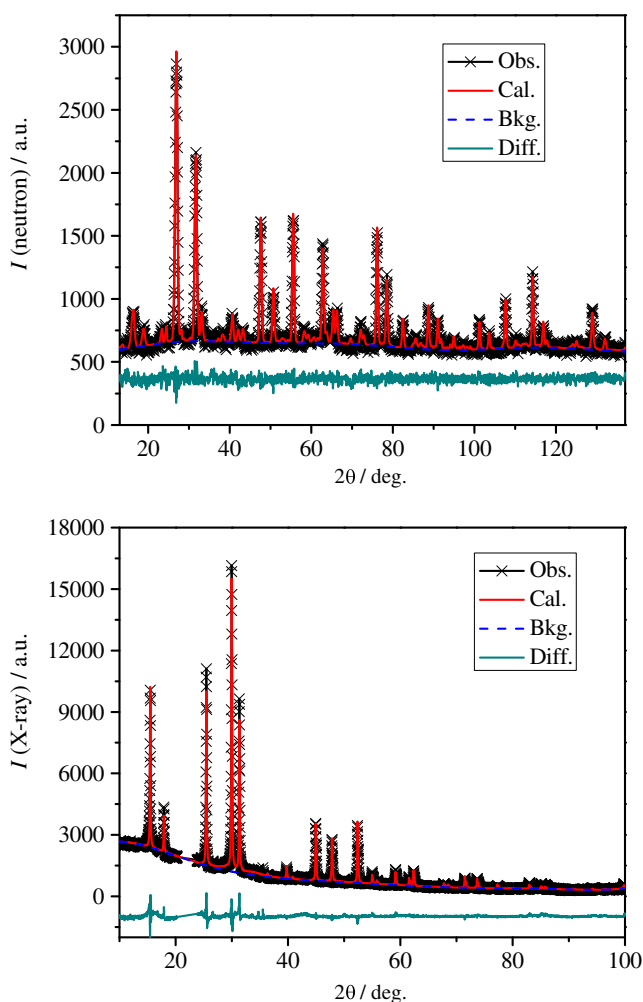
Fig. 3 Rietveld fits of simultaneously refined structural models to NPD (*top*) and XRPD (*bottom*) data for Li$_6$PS$_5$Cl

site 1" (63% S, 37% Cl) and "anion site 2" (63% Cl, 37% S). The halide ion in this case seems to slightly prefer the site occupied by S^{2-} in Li$_6$PS$_5$I.

A similar anion disorder to that of Li$_6$PS$_5$Cl is observed for Li$_6$PS$_5$Br, where Br is distributed over "anion site 1" (43% S, 57% Br) and "anion site 2" (43% Br, 57% S). Note

Table 1 Atomic coordinates, isotropic atomic displacement parameters (U_{iso}) and site occupancy factors of Li$_6$PS$_5$I derived from simultaneous refinement using XRPD and NPD data

Atom	x	y	z	SOF	U_{iso} (Å^2)
Li(1)	0.3005	0.3005	−0.0302	0.31	0.031
Li(2)	0.2500	0.2500	−0.0168	0.39	0.031
P	0.5000	0.5000	0.5000	1	0.014
I(1)	0.0000	0.0000	0.0000	1	0.026
S(2)	0.7500	0.7500	0.7500	1	0.018
S(3)	0.1200	−0.1200	0.6200	1	0.018

$R_{wp}=0.055$

Table 2 Atomic coordinates, isotropic atomic displacement parameters (U_{iso}) and site occupancy factors of Li$_6$PS$_5$Cl derived from simultaneous refinement using XRPD and NPD data

Atom	x	y	z	SOF	U_{iso} (Å^2)
Li(1)	0.3161	0.3161	−0.0229	0.44	0.088
P	0.5000	0.5000	0.5000	1	0.046
Cl(1)	0.0000	0.0000	0.0000	0.37	0.016
S(1)	0.0000	0.0000	0.0000	0.63	0.016
S(2)	0.7500	0.7500	0.7500	0.37	0.041
Cl(2)	0.7500	0.7500	0.7500	0.63	0.041
S(3)	0.1211	−0.1211	0.6211	1	0.058

$R_{wp}=0.044$

that, in contrast to Li$_6$PS$_5$Cl, "anion site 1" in Li$_6$PS$_5$Br has now a slight preference for the halide ion. The lithium distribution in Li$_6$PS$_5$Br, as for X = I, can be described by a distribution over Li(1) and Li(2) sites, yet with a more pronounced preference for the Li(1) site.

The temperature dependence of the lattice constants is plotted in Fig. 4. It should be noted that the observed coefficients of linear thermal expansion are 3.4×10^{-5} K^{-1}, 3.1×10^{-5} K^{-1}, 2.5×10^{-5} K^{-1} for Li$_6$PS$_5$Cl, Li$_6$PS$_5$Br, and Li$_6$PS$_5$I, respectively, showing a clear decrease from X = Cl to X = I in the opposite direction to the bond softness.

Figure 5 shows the variation of the apparent distance between P and S(3) as a function of temperature for the three studied compounds. For X = Cl, an expected slight increase of the bond length with rising temperature was observed, while for X = I and X = Br an apparent decrease of the P–S bond length was observed at elevated temperatures. Such an apparent bond shortening with rising temperature is most likely a sign of large angle-hindered rotations of the nearly rigid PS$_4^{3-}$ in these structures. It may be assumed that the larger Br$^-$ and I$^-$ expand the structure sufficiently to promote such librations, while the more

Table 3 Atomic coordinates, isotropic atomic displacement parameters (U_{iso}) and site occupancy factors of Li$_6$PS$_5$Br derived from simultaneous refinement using XRPD and NPD data

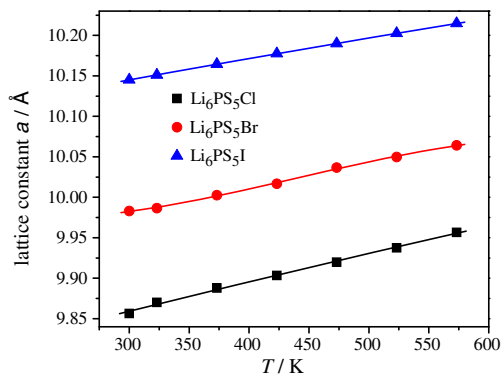| Atom	x	y	z	SOF	U_{iso} (Å^2)
Li(1)	0.3118	0.3118	−0.0216	0.43	0.066
Li(2)	0.2500	0.2500	−0.0188	0.14	0.066
P	0.5000	0.5000	0.5000	1	0.026
Br(1)	0.0000	0.0000	0.0000	0.57	0.050
S(1)	0.0000	0.0000	0.0000	0.43	0.050
S(2)	0.7500	0.7500	0.7500	0.57	0.035
Br(2)	0.7500	0.7500	0.7500	0.43	0.035
S(3)	0.1193	−0.1193	0.6193	1	0.078

$R_{wp}=0.049$

Fig. 4 Variation of lattice constants with temperature. Errors are smaller than *symbols*

compact structure for X = Cl⁻ impedes the librations. This could also explain the reduced thermal expansion of the more compact Li_6PS_5Cl structure.

Scanning electron microscopy (SEM) images of Li_6PS_5Br samples show the formation of a dense glass ceramic with crystallites of about 100 nm in diameter from the essentially amorphous ball-milled sample (Fig. 6).

The temperature-dependent ionic conductivity of the samples, as determined from impedance spectra, shows Arrhenius-type behaviour (Fig. 7). Ball-milled Li_6PS_5Cl, Li_6PS_5Br and Li_6PS_5I samples exhibit ionic conductivities of 3.3×10^{-5}, 3.2×10^{-5} and 2.2×10^{-4} S cm^{-1}, with activation energies (E_A) of 0.38, 0.32 and 0.26 eV, respectively. The ionic conductivities of annealed crystalline compounds are 7.4×10^{-4}, 7.2×10^{-4} and 4.6×10^{-7} S cm^{-1} with E_A 0.11, 0.17 and 0.25 eV, respectively. Hence the conductivity of argyrodite-type Li_6PS_5I is ca. 500 times lower than that of the ball-milled (essentially amorphous) material, but the activation energy remains nearly unchanged. In contrast, the argyrodite phases Li_6PS_5Cl and Li_6PS_5Br show an increase in conductivity by a factor of ~20 and a pronounced decrease in activation energy as a result of crystallization.
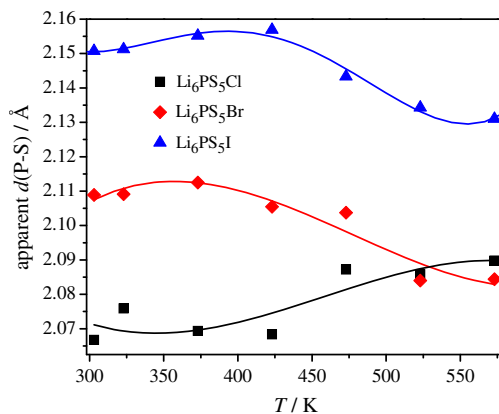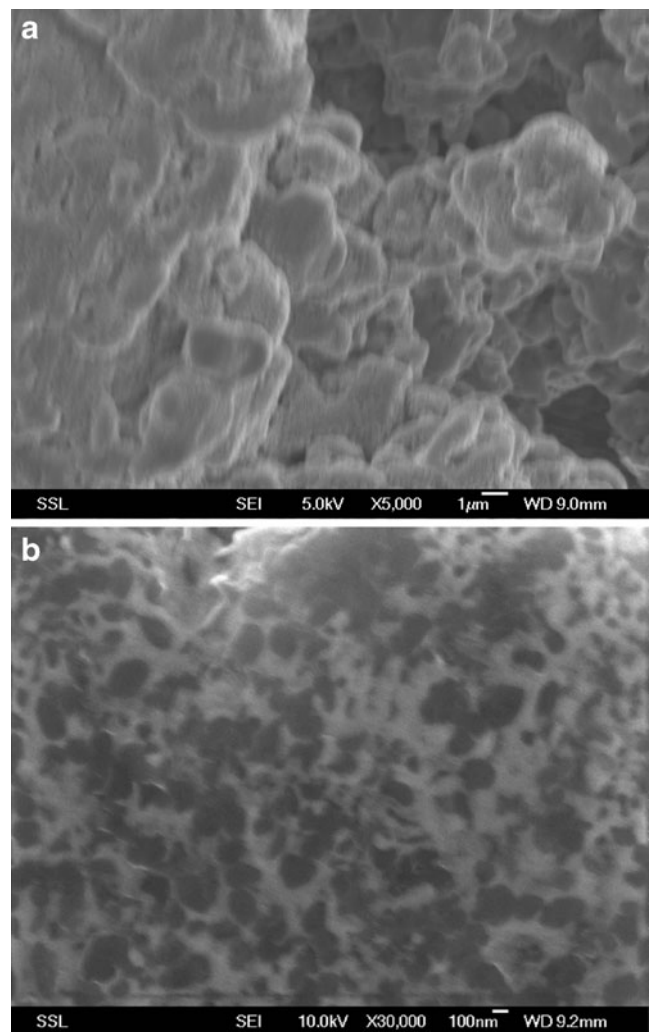

Fig. 6 SEM images of Li_6PS_5Br (**a**) before and (**b**) after heat treatment

The key difference between the structures for X = I and for X = Cl, Br seems to be the anion disorder observed for the lighter halides, which may induce the high conductivity and low activation energy. Low-temperature ionic conductivity studies are in progress in our laboratory to determine the effect of order–disorder transitions on the ion transport. Figure 7 compares Li$^+$ ion migration pathways in idealized Li_6PS_5X argyrodite structures with X = Cl and I with ordered anion arrangements. Generally, the three-dimensional pathway network for long-range (dc) ionic conduction in all Li_6PS_5X phases consists of interconnected low-energy local pathway "cages" around anion sites 1 and 2. More specifically, these cages and their interconnectivity differ for the compounds with different halide ions. For X = Cl (Fig. 8a), the sites of lowest energy agree with the experimentally refined half-occupied Li(1) site. The lowest energy short-range pathway then interconnects three such partially occupied Li sites via three interstitial sites, forming a pathway hexagon (E_A=0.10 eV). Four such hexagons are

Fig. 5 Variation of P–S (3) bond distance, *d*(P–S), with temperature
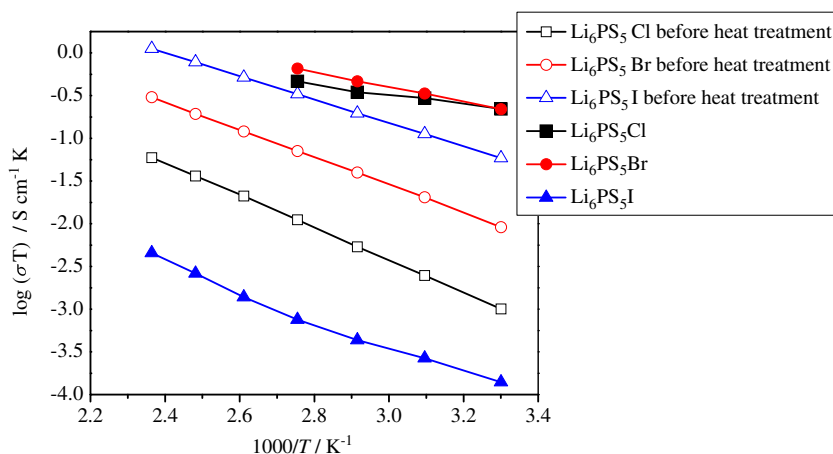
then interconnected at a slightly higher energy threshold, via a second interstitial site, to form an extended pathway cage around "anion site 1" (E_A=0.18 eV) and the three-dimensional long-range pathway network in the anion-ordered structure is established by a direct connection between the cages (E_A=0.32 eV) that is equivalent to another set of pathway cages around "anion site 2". In the anion-disordered Rietveld-refined structure, it may be assumed that the lower energy long-range pathways are possible by networks of cages around halide ions, whereas for the anion-ordered phase, long-range pathways alternate between the environments of sulphide and halide ions.

For the case of Li_6PS_5I (with an ordered anion arrangement), the experimental studies suggest a more disordered Li distribution, as shown here in accordance with [5], with Li(1)–Li(2)–Li(1) triplet sites. In our BV model, it is obvious that the Li(1) site still exhibits the lowest E(Li) and the Li(2) site in between pairs of Li(1) sites are included as a local path resulting in a very low energy threshold (ca. 0.13 eV), though Li(2) appears not to be a local minimum of E(Li), which is also in line with the difference Fourier plot shown in [18]. Experimental NMR data find even lower activation energy of 0.043 eV for unspecified local hops [5]. Six of these dumbbell-like local pathways (which correspond to the intercage pathways in Li_6PS_5Cl) form a pathway cage around the S^{2-} on "anion site 2" with E_A=0.18 eV. The cages are finally interconnected via an interstitial site giving E_A=0.33 eV in remarkable
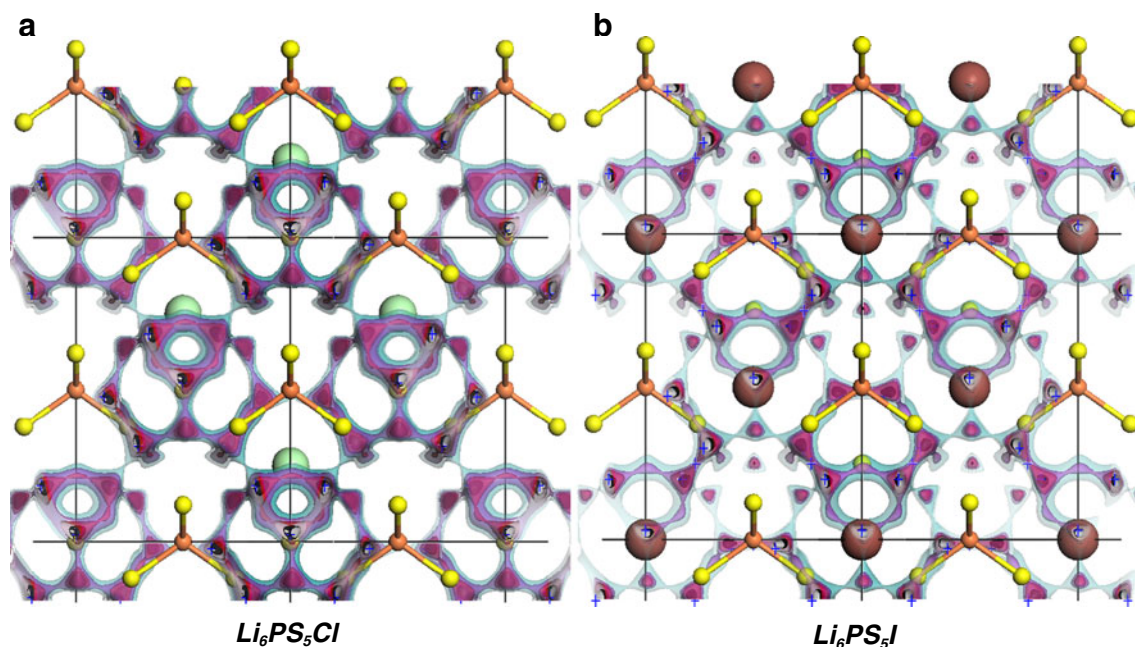

Fig. 8 Li$^+$ migration pathways in Li_6PS_5X, where X = Cl (**a**) or X = I (**b**), for different energy thresholds characterizing equilibrium sites (*black*), first local Li$^+$ paths (*red*), extended local Li$^+$ pathway cages (*magenta*) and long-range Li$^+$ migration pathways (*light blue*). Note that pathways are different in detail (cf. text)

agreement with the experimental value 0.32 eV from low temperature impedance spectroscopy and 0.30 eV from molecular dynamics (MD) simulations [19]. MD simulations also suggest 0.14 eV for a localized motion close to the BV prediction of E_A for Li(1)–Li(2)–Li(1) pathways.

This pathway model for Li_6PS_5I is essentially identical to the model proposed by Deiseroth et al. [6] based on crystal–geometrical considerations, but it should be noted that in contrast to what the authors implied, we find that argyrodites containing different halide ions exhibit differences in their Li^+ ion transport pathways that may be traced back to the difference in the halide/sulphide anion size ratio as well as the difference in the degree of anion ordering.

The characteristics of Li^+ pathways in Li_6PS_5Br appear to mix features of Li^+ pathways found in the compounds with X = Cl and X = I. Again, there is a clear disorder over Li(1) sites (the experimental structure determination again suggests a Li(1)–Li(2)–Li(1) triplet). The lowest energy local pathway interconnecting these sites is a hexagon of 3 Li(1) sites and three interstitial sites as in Li_6PS_5Cl (E_A=0.14 eV). The local pathway cage around anion sites 1 and 2 forms at practically the same energy threshold, $E_A \approx 0.26$ eV. It should be noted that the structural model and hence the BV model of Li_6PS_5Br may be less accurate as the halide content is not exactly 1.

It might be noteworthy that analogous oxide argyrodites Li_6PO_5X (X = Cl, Br) have also been reported recently [20]. Due to the different positions of oxide ion O(2) in Li_6PO_5X relative to the S(2) position in Li_6PS_5X, pathway cages and long-range pathways found for the oxide argyrodites are fundamentally different from those in the Li_6PS_5X series, causing significantly higher activation energies in bond valence models for local (0.4 eV) and long-range pathways (0.57 eV) in Li_6PO_5Cl and the absence of interstitial sites in these pathways. Therefore, it can be understood why the oxide analogues show orders of magnitude lower conductivity ($\sim 10^{-9}$ S cm^{-1} at ambient temperature and experimental activation energy of 0.66 eV).

Summary

Li_6PS_5X argyrodite structures were prepared by mechanical milling followed by annealing of the samples, allowing significantly faster synthesis than the previously reported procedures. The obtained crystalline phases show ionic conductivity of the order of 7×10^{-4} S cm^{-1} at ambient temperature for X = Cl or Br. From the synopsis of the structural studies and the bond valence models, it may be concluded that fast ion transport in the argyrodites requires that the packing is determined by the PS_4^{3-} anions and thereby smaller halide ions enhance the ion mobility,

whereas for Li_6PS_5I the large iodide anions effectively impede the interconnection of local pathway cages. Large-angle libration motion of PS_4^{3-} was observed but did not contribute to the Li^+ motion. It could be clarified that the extremely low activation energies reported from NMR studies refer to hops within extended local Li^+ pathway cages that are not directly relevant for the dc conductivity, unless the pathway cages are interconnected.

Due to the high ionic conductivity of Li_6PS_5Cl and Li_6PS_5Br at room temperature, these compounds are of technological interest as some of the best solid electrolytes for high-energy all-solid-state battery applications. We are currently undertaking in situ neutron diffraction experiments to explore the detailed evolution of anion disorder during crystallization and ways to control the degree of disorder via the annealing conditions.

References

1. Minami K, Mizuno F, Hayashi K, Tatsumisago M (2007) Solid State Ionics 178:837–841
2. Saienga J, Martin SW (2008) J Non-Cryst Solids 354:1475–1486
3. Prasada Rao R, Seshasayee M (2006) J Non-Cryst Solids 352:3310–3314
4. Beeken RB, Garbe JJ, Gillis JM, Petersen NR, Podoll BW, Stoneman MR (2005) J Phys Chem Solid 66:882–886
5. Deiseroth H-J, Kong S-T, Eckert H, Vannahme J, Reiner C, Zaiß T, Schlosser M (2008) Angew Chem Int Ed 47(4):755–758
6. Deiseroth H-J, Maier J, Weichert K, Nickel V, Kong S-T, Reiner C (2011) Z Anorg Allg Chem 637:1287–1294
7. Kuhs WF, Nitsche R, Scheunemann K (1979) Mat Res Bull 14:241–248
8. Larson AC, von Dreele RB (2000) General Structure Analysis System (GSAS). Report LAUR 86–748; Los Alamos National Laboratory, Los Alamos, NM
9. Toby BJ (2001) J Appl Crystallogr 34:210–213
10. Adams S (2000) J Power Source 159:200–204
11. Adams S (2001) Acta Crystallogr B Struct Sci 57:278–287
12. Adams S, Swenson J (2004) Solid State Ionics 175:665–669
13. Adams S (2006) Solid State Ionics 177:1625–1630
14. Adams S, Prasada Rao R (2009) Phys Chem Chem Phys 11:3210–3216
15. Prasada Rao R, Tho TD, Adams S (2010) Solid State Ionics 181:1–6
16. Adams S, Prasada Rao R (2011) Phys Stat Sol A 208(8):1746–1753
17. Prasada Rao R, Adams S (2011) Phys Stat Sol A 208(8):1804–1807
18. Kong S-T, Deiseroth H-J, Reiner C, Gün Ö, Neumann E, Ritter C, Zahn D (2010) Chem Eur J 16:2198–2206
19. Pecher O, Kong S-T, Goebel T, Nickel V, Weichert K, Reiner C, Deiseroth H-J, Maier J, Haarmann F, Zahn D (2010) Chem Eur J 16:8347–8354
20. Kong S-T, Deiseroth H-J, Maier J, Nickel V, Weichert K, Reiner C (2010) Z Anorg Allg Chem 636:1920–1924